applied sciences

MDPI

Article

Construction Mechanical Characteristics of TBM Pilot and Enlargement Method for Ventilation Tunnel of Wuhai Pumped Storage Power Station

Chuanjun Fan [1,2], Jianmin Qin [1,2,*] and Guixuan Wang [3]

[1] Key Laboratory for Prediction & Control on Complicated Structure System of the Education Department of Liaoning Province, Dalian University, Dalian 116622, China; fanchuanjun2024@163.com
[2] College of Civil Engineering and Architecture, Dalian University, Dalian 116022, China
[3] College of Environment Sciences and Engineering, Dalian Maritime University, Dalian 116026, China; tumuxinxi@163.com
* Correspondence: qinjianmin@dlu.edu.cn

Abstract: Investigating the construction mechanics of a ventilation tunnel using the TBM (Tunnel Boring Machine) pilot and enlargement method with reliable rock mechanics parameters ensures the safety of on-site excavation operations. Leveraging the construction project of the ventilation tunnel at the Wuhai Pumped Storage Power Station, TGP sidewall forecasting was employed to explore the geological conditions within a 50 m range of the tunnel's side. A systematic study of the construction mechanics of the TBM pilot and enlargement method was conducted, along with corresponding construction recommendations and engineering applications. This research indicates that sidewall forecasting can supplement the deficiencies in geological exploration reports, with excavation revealing conditions consistent with the forecast. Deformation at the interface, including the arch crown and sidewall, mainly concentrates during the construction phase from the completion of full-section excavation to the beginning of expansion. As the working face advances, the upper rock mass within the ventilation tunnel outline experiences tension, with stress concentration in the shoulder and bottom corner rock masses. The plastic zone before expansion primarily concentrates within the ventilation tunnel outline, shifting to the sidewall after expansion, with the left shoulder's plastic zone depth slightly exceeding that of the right. The proposed method effectively ensures construction safety, and the research findings have valuable implications for similar projects.

Keywords: TBM pilot and enlargement method; TGP sidewall forecasting; Hoek–Brown strength criterion; rock stability; Wuhai pumped storage power station

Citation: Fan, C.; Qin, J.; Wang, G. Construction Mechanical Characteristics of TBM Pilot and Enlargement Method for Ventilation Tunnel of Wuhai Pumped Storage Power Station. *Appl. Sci.* **2024**, *14*, 1829. https://doi.org/10.3390/app14051829

Academic Editor: Weon Gyu Shin

Received: 3 January 2024
Revised: 15 February 2024
Accepted: 19 February 2024
Published: 23 February 2024

1. Introduction

To realize the net-zero carbon pledge, urgent reforms must be carried out to optimize the energy structure by building a low-carbon, clean and efficient energy system, taking robust renewable energy substitution actions and boosting the development of clean energy such as hydro and solar energy. In the new power system with new energy, the pumped storage power station plays an extremely important role [1]. In 2019, the global installed capacity of pumped storage was 158 million kW, accounting for more than 94% of the global installed energy storage capacity, and pumped storage dominated energy storage. Pumped storage power stations are often located in complex geological conditions. It is a concerning issue how the mechanical behavior of the underground cavern is affected by construction, environment and other factors [2–4].

Geophysical methods, such as seismic wave methods like Time-Gated Probing (TGP) and Time-Shift Profiling (TSP), are commonly used for geological exploration [5]. These methods, especially TGP and TSP, are widely applied in tunnel geological exploration due to their advantages of high energy and long propagation distances. Currently, TGP or TSP

is primarily used for advanced geological forecasting [6–8]. After the excavation of the cavern, the side wall rock mass bears the load transmitted from the arch rock mass. If the estimation of the side wall rock mass is insufficient, it can lead to engineering disasters caused by an inadequate initial support-bearing capacity, resulting in side wall extrusion and overall settlement of the arch rock mass. TGP side wall forecasting for the location of joint fissures in the side wall rock mass can complement the limitations of geological exploration reports and enhance the safety of tunnel construction.

It is well known that using reasonable rock mass mechanical parameters is crucial for studying the construction mechanics of underground caverns. While field tests for obtaining rock mass strength parameters are the most direct and reliable, they are not suitable for extensive use in engineering due to the consumption of significant human and material resources [9]. Elastic wave testing has economic advantages, rapidity, flexible layout of measurement points, and a large number of measurement points compared to in situ tests. The relationship between wave velocity and rock mass parameters has been gradually established by many researchers [10], laying the foundation for predicting rock mass parameters based on wave velocity and numerical simulation.

Drill and blast methods are flexible and cost-effective, while Tunnel Boring Machine (TBM) methods have the advantages of safety and speed compared to drill and blast methods [11]. TBM tunneling involves the initial construction of a pilot tunnel and subsequent enlargement using drill and blast methods. This method has received widespread attention from scholars, and various studies have discussed the advantages and disadvantages of TBM tunneling compared to drill and blast methods [12–16]. Some research has focused on the impact of the TBM pilot tunnel position and dimensions on tunnel deformation [17]. In this study, based on TGP side wall forecasting to detect the geological conditions of the excavation section, rock mechanics parameters were predicted using measured wave velocities according to the Hoek–Brown criterion. A three-dimensional simulation model of the entire excavation process for both full-section excavation and TBM pilot tunnel enlargement was established based on the predicted rock mechanics parameters and the actual conditions of tunnel construction. The study investigated the mechanical behavior of the surrounding rock at the interface between full-section excavation and TBM pilot tunnel enlargement as the construction progressed and proposed corresponding design and construction suggestions.

2. Project Overview

The ventilation tunnel is 1870 m long, with an average slope of 1.1%. The tunnel entrance is on the south side of the Y1 highway, with an elevation of 1162.0 m. The terminal enters the auxiliary plant ventilation layer from the left side of the underground plant, with an elevation of 1143.2 m. The analysis section covers the overlying rock layer thickness, at a surface elevation 12,451,336 m and a tunnel overlying rock thickness of 80,176 m. The surrounding rock of the tunnel mainly consists of mudstone-banded limestone, medium-thick-layer leopard skin limestone, and shale from the fifth layer ($\in_2 x^5$) to the second layer ($\in_2 x^2$) of the slightly weathered Xuzhuang Formation. The shale is classified as soft rock, and the surrounding rock is categorized as Class IV. The mudstone-banded limestone and medium-thick-layer leopard skin limestone sections are classified as Class III, and in some areas, the rock mass is Class IV due to local structural development. The geological longitudinal section is shown in Figure 1.

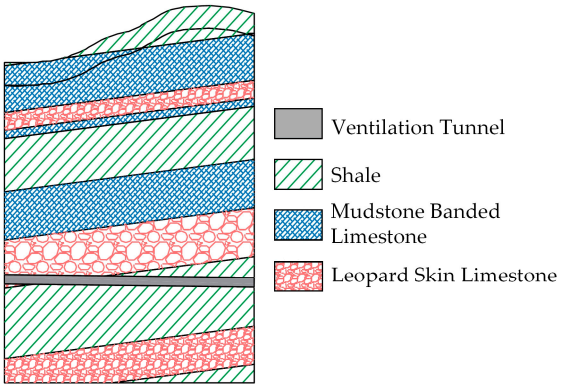

Figure 1. Regional geological profile.

3. Ventilation Tunnel Side Wall Forecast

3.1. Side Wall Forecast Data Collection

Side wall forecasting was conducted in the pilot tunnel, with a forecast mileage from TFD 1 + 230 to TFD 1 + 322, covering a distance of 92 m. In this survey, 48 boreholes were arranged on each side of the tunnel, totaling 96 boreholes, as shown in Figure 2. The spacing between the excitation boreholes in the direction of the tunnel mileage increase was 2 m. The first pair of receiving boreholes was located 10 m from the nearest excitation borehole, and the second set of receiving boreholes coincided with the position of the first set of boreholes at TFD 1 + 19. All the boreholes were located 1 m above the tunnel bottom. The depth of both the excitation and receiving boreholes was 1.5 m, and the arrangement of the excitation and receiving boreholes is illustrated in Figure 3.

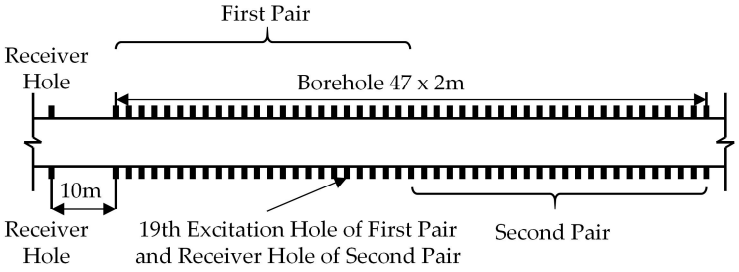

Figure 2. Layout drawing of the survey line.

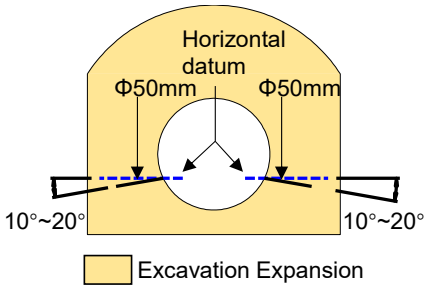

Figure 3. Cross-section of the drill layout.

3.2. Interpretation of Side Wall Forecasting Results

The seismic wave data collected on-site were imported into post-processing software to obtain the side wall reflection interface diagram, as shown in Figures 4 and 5. The horizontal axis represents the mileage position, and the vertical axis represents the depth of the side wall rock layers. Based on the distribution of the reflection interfaces in the figures, the following conclusions can be drawn:

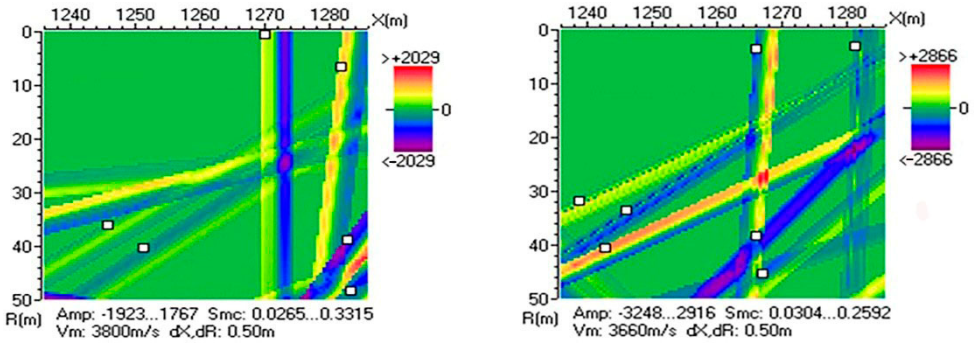

(**a**) (**b**)

Figure 4. TFD 1 + 230 to TFD 1 + 276 reflective interface: (**a**) left Wall from TFD 1 + 230 to TFD 1 + 276, and (**b**) right Wall from TFD 1 + 230 to TFD 1 + 276.

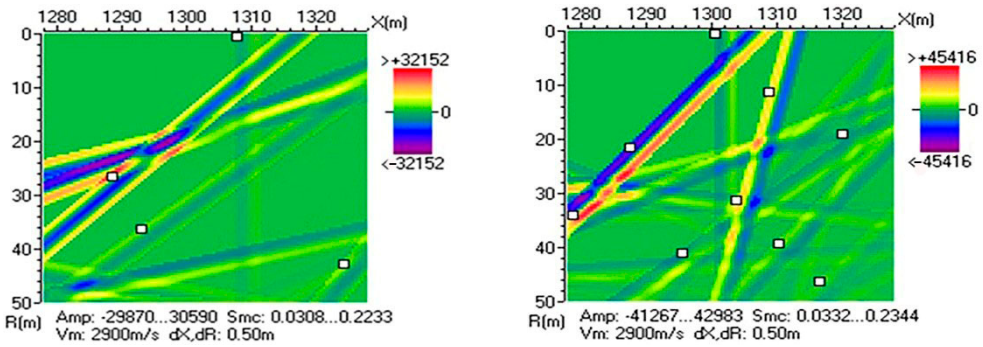

(**a**) (**b**)

Figure 5. TFD 1 + 276 to TFD 1 + 322 reflective interface: (**a**) left Wall from TFD 1 + 276 to TFD 1 + 322, and (**b**) right Wall from TFD 1 + 276 to TFD 1 + 322.

From Figure 4a,b, it can be observed that in the TFD 1 + 230 to TFD 1 + 260 section, there are no significant reflection interfaces within a depth of 20 m from the side wall. The rock mass condition is relatively good in this section, and after 20 m, negative reflection (blue) interfaces intersect, indicating that joint fissures are more developed at this location. From Figure 4a,b, it can be seen that in the TFD 1 + 270 and beyond, the number of negative reflection (blue) interfaces increases. It is inferred that there is a developed fault zone at this location, and the rock mass is relatively fractured. The reflection interfaces on the right wall are denser than on the left wall, suggesting a poorer rock mass condition on the right wall. It is recommended to strengthen monitoring in this section during construction.

From Figure 5a, it can be seen that in the vicinity of TFD 1 + 276 to TFD 1 + 300, there are no significant reflection interfaces within a 10 m depth from the side wall, indicating a relatively good rock mass condition. Within a range of 20–40 m, there are two significant negative reflection (blue) interfaces. Beyond TFD 1 + 300, the number of negative reflection (blue) interfaces increases, suggesting developed joint fissures at these locations, and the integrity of the rock mass deteriorates. It is recommended to strengthen monitoring in this section during construction.

From Figure 5b, it can be seen that the negative reflection (blue) interfaces are dense after TFD 1 + 300, indicating a relatively poor overall rock mass condition compared to the TFD 1 + 276 to TFD 1 + 300 section. It is inferred that joint fissures are more developed after TFD 1 + 300, and the rock mass is relatively fractured. It is recommended to strengthen monitoring in this section during construction.

3.3. Comparison of Excavation Exposure and Forecast Results

Side wall forecasting was conducted for TFD 1 + 230 to TFD 1 + 322, and the forecast results were compared with the actual conditions after excavation, as shown in Table 1. The

exposed rock mass conditions during excavation generally matched the forecast conditions, indicating that side wall forecasting complemented the limitations of geological survey reports regarding joint fissures.

Table 1. TGP results compared with actual results.

Forecasted Station Number	Forecast of Sidewall Conditions	Actual Conditions after Excavation
TFD 1 + 260~TFD 1 + 280	After TFD 1 + 270, there is an increase in negative reflection interfaces, indicating poor integrity of the surrounding rock at this location.	The intersection of three sets of fractures in the same stratigraphic plane (interlayer fractures) locally forms potential unstable blocks, and the width of the fracture surfaces is mostly slightly widened.
TFD 1 + 290~TFD 1 + 322	After TFD 1 + 300, the development of structural fracture zones is observed, and the integrity of the surrounding rock is poor.	The surrounding rock in this section mainly exhibits a laminated structure, with poor integrity.

4. Prediction of Side Wall Rock Mass Mechanical Parameters

4.1. Calculation of Rock Mass Wave Velocity

TGP geological forecasting can provide the longitudinal and transverse wave velocities of the rock mass. The calculation of the longitudinal and transverse wave velocities is similar to the cross-hole acoustic wave method. With the spacing between the excitation boreholes known, the time difference between the wave starting times at adjacent measurement points was obtained. The wave velocity of the rock mass between adjacent excitation boreholes was calculated by dividing the spacing between excitation boreholes by the time difference between wave starting times.

4.2. Estimation of Rock Mass Parameters

4.2.1. The Relationship between Rock Mass Wave Velocity and Uniaxial Compressive Strength of Rocks

Wang [18] proposed a relationship between the rock mass longitudinal wave velocity and the uniaxial compressive strength of rocks based on more than 20,000 sets of rock test data collected from 11 railway construction projects in southern China.

$$V_{\mathrm{pr}} = 1150\sigma_{\mathrm{ci}}^{\frac{1}{3}} \tag{1}$$

In the equation: V_{p} represents the longitudinal wave velocity of rocks in m/s, and σ_{ci} represents the uniaxial compressive strength of rocks in MPa. It should be noted that σ_{ci} needs to satisfy the condition of 0.5 MPa $\leq \sigma_{\mathrm{ci}} \leq$ 300 MPa.

The expression for the relationship between the longitudinal wave velocity of rocks V_{p} and the uniaxial compressive strength of rocks σ_{ci} can be derived by substituting the rock mass integrity index into Equation (1) [18].

$$V_{\mathrm{p}} = 1150k_{\mathrm{v}}^{\frac{1}{2}}\sigma_{\mathrm{ci}}^{\frac{1}{3}} \tag{2}$$

In the equation: V_{p} represents the longitudinal wave velocity of rocks in m/s, σ_{ci} represents the uniaxial compressive strength of rocks, and K_{v} represents the rock mass integrity index. The rock mass integrity index can be obtained using the rock mass volumetric joint number J_{v} according to the relationship shown in Table 2 [19]. The fitted expression for the rock mass integrity index is given by Equation (3) [20].

$$K_{\mathrm{v}} = -0.01834J_{\mathrm{v}}+0.7618 \tag{3}$$

Table 2. Correspondence between K_v and J_v.

J_v (cracks/m^3)	<3	3~10	10~20	20~35	≥35
K_v	>0.75	0.75~0.55	0.55~0.35	0.35~0.15	≤0.15

4.2.2. The Hoek–Brown Criterion

In 2002, E. Hoek et al. [21] introduced the geological strength index *GSI* and disturbance parameter *D* as modifications to the Hoek–Brown criterion. The modified Hoek–Brown criterion is expressed as follows:

$$\sigma_1 = \sigma_3 + \sigma_{ci}\left(m_b\frac{\sigma_3}{\sigma_{ci}} + s\right)^a \tag{4}$$

In the equation, σ_1 and σ_3 represent the maximum and minimum principal stresses at rock failure, respectively. σ_{ci} is the uniaxial compressive strength of the rock. m_b, s, and a are functions related to the geological strength index *GSI* and disturbance parameter *D*. The geological strength index *GSI* can be expressed in terms of the rock's longitudinal wave velocity V_p. Therefore, the final expression [22] is:

$$\left.\begin{aligned} m_b &= m_i \exp\left(\tfrac{40V_p-290}{84-24D}\right) \\ s &= \exp\left(\tfrac{40V_p-290}{27-9D}\right) \\ a &= \tfrac{1}{2} + \tfrac{1}{6}\left(e^{\frac{-(8V_p+2)}{9}} - e^{\frac{-20}{3}}\right) \end{aligned}\right\} \tag{5}$$

In the equation, m_i represents the Hoek–Brown constant, which is derived by P. Marinos et al. [23]. V_p is the longitudinal wave velocity of the rock, measured in km/s. *D* is the disturbance coefficient, which can be expressed as follows [22]:

$$D = 1 - k_v \tag{6}$$

In the equation, K_v represents the rock mass integrity index, which can be calculated using Equation (3).

4.2.3. The Uniaxial Compressive Strength of the Rock Mass

The expression for the uniaxial compressive strength of the rock mass can be obtained by setting σ_3 = 0 in Equation (3), as given in reference [21].

$$\sigma_c = \sigma_{ci}s^a \tag{7}$$

The expression for the uniaxial tensile strength of the rock mass σ_t can be obtained by setting $\sigma_1 = \sigma_3 = \sigma_t$ in Equation (3), as given in reference [21].

$$\sigma_t = -\frac{s\sigma_{ci}}{m_b} \tag{8}$$

4.2.4. The Compressive Strength of the Rock Mass

By defining the minimum principal stress within a certain range, the equivalent internal friction angle and cohesion of the Mohr–Coulomb criterion can be obtained [21]. The expression is as follows:

$$\phi = \sin^{-1}\left[\frac{1}{\frac{(1+a)(2+a)}{3am_b\left(s+m_b\sigma'_{3n}\right)^{a-1}}+1}\right] \tag{9}$$

$$c = \frac{\sigma_{ci}[(1+2a)s + (1-a)m_b\sigma'_{3n}](s + m_b\sigma'_{3n})^{a-1}}{(1+a)(2+a)\sqrt{1 + \left[6am_b(s + m_b\sigma'_{3n})^{a-1}\right]/(1+a)(2+a)}} \quad (10)$$

where ϕ and c represent the equivalent internal friction angle and cohesion, respectively, with the unit of the equivalent internal friction angle being degrees. σ'_{3n} can be expressed by the following equation:

$$\sigma'_{3n} = \frac{\sigma'_{3max}}{\sigma_{ci}} \quad (11)$$

The σ'_{3n} for tunnel engineering, as proposed by E. Hoek et al. [21], can be expressed by the following equation:

$$\frac{\sigma'_{3max}}{\sigma'_{cm}} = 0.47\left(\frac{\sigma'_{cm}}{\gamma H_t}\right)^{-0.94} \quad (12)$$

In the equation, σ'_{cm} represents the compressive strength of the rock mass, γ represents the unit weight of the rock mass, and H_t represents the depth of the tunnel. When $\sigma_t < \sigma_3 < 0.25\sigma_c$, the compressive strength of the rock mass can be expressed by the following equation [21]:

$$\sigma'_{cm} = \sigma_{ci}\frac{[m_b + 4s - a(m_b - 8s)](m_b/4 + s)^{a-1}}{2(1+a)(2+a)} \quad (13)$$

4.2.5. Calculation of Rock Mass Deformation Parameters

Since the rock mass wave velocity obtained from the sidewall prediction calculation of TGP is the disturbed rock mass wave velocity, the relationship between the rock mass longitudinal wave velocity and the rock mass deformation modulus is obtained using the improved method proposed by Li et al. [22].

$$E_m = 10^{\frac{V_p - 0.5}{3}} \quad (14)$$

In the equation: E_m represents the deformation modulus of the rock mass in GPa, and V_p represents the longitudinal wave velocity of the rock mass in km/s.

4.2.6. The Relationship between Wave Velocity and Rock Density

Previous studies have shown that there is a polynomial relationship between rock density and rock compressional wave velocity V_{pr}. By using Equation (1) to calculate the rock compressional wave velocity V_{pr} and substituting it into the following expression, the density of the rock can be estimated. The expression is [24]:

$$\rho = mV_{pr}{}^2 + nV_{pr} + l \quad (15)$$

In the equation: ρ represents the estimated rock density in g/cm^3; V_{pr} represents the rock compressional wave velocity in km/s; m, n, and l are all constants that can be obtained from Table 3.

Table 3. Partial polynomial constants.

Lithology	*m*	*n*	*l*
Shale	−0.0261	0.373	1.458
Limestone	−0.0296	0.461	0.963

4.2.7. The Relationship between Young's Modulus and Poisson's Ratio

According to extensive field tests and engineering experience, there is a certain relationship between Young's modulus and Poisson's ratio [25]. The expression is as follows:

$$\mu = 0.4 - 0.05\lg\frac{E_{\mathrm{m}}}{2} \tag{16}$$

where μ represents the Poisson's ratio of the rock mass, and E_m represents the deformation modulus of the rock mass in MPa.

Due to the complex geological conditions in the vicinity of the ventilation tunnel, there is a significant variation in wave velocity between adjacent blast holes. Therefore, in this study, the areas with higher and lower wave velocities are divided into different calculation segments. The average wave velocity within each calculation segment is used for the calculations. The results of the segmented calculations are shown in Table 4.

Table 4. Mechanical parameters of the surrounding and supporting structures.

Materials/Location	Density/g·cm^{-3}	E_{m}/GPa	μ	ϕ/°	c/MPa
Shale	2.65	0.8	0.35	27	0.4
Muddy limestone	2.69	6	0.25	42	1.2
Leopard skin limestone	2.69	9	0.25	48	1.5
Shotcrete	2.5	23	0.2	-	-
Equivalent concrete	2.5	30.97	0.2	-	-
Anchor bolt	7.85	200	0.3	-	-
L1	2.44	0.6	0.31	23	0.29
L2	2.4	0.5	0.32	22	0.38
L3	2.34	0.4	0.33	21	0.52
L4	2.32	0.4	0.33	21	0.56
R1	2.43	0.6	0.31	23	0.31
R2	2.38	0.5	0.32	22	0.43
R3	2.32	0.4	0.33	21	0.56
R4	2.30	0.4	0.33	20	0.61

5. Numerical Model Establishment and Results Analysis

5.1. Numerical Model Establishment

According to the actual excavation conditions on-site, excavation was conducted simultaneously from the left and right boundaries toward the dividing interface. The left side of the dividing interface was excavated using the full-section method (labeled as ① in Figure 6a), while the right side of the dividing interface initially used a TBM to create a pilot tunnel (labeled as ② in Figure 6a). When the working faces of both methods reached the junction interface, the right side of the dividing interface started reverse excavation (labeled as ③ in Figure 6a) toward the right boundary of the model. This adjustment was made to ensure that the dimensions of the ventilation shaft met the design requirements. The relative positions of the pilot tunnel and the ventilation shaft are illustrated in Figure 6b.

Midas GTS NX was used in this study to simulate the excavation process of the ventilation shaft, and the numerical model is shown in Figure 7. To mitigate the boundary effects, [26,27], the width of the model on both the left and right sides was set to 100 m. The longitudinal length of the model was 178 m. The minimum distance from the bottom edge of the ventilation shaft to the model bottom was 50 m, and the model's upper surface was set to the terrain surface. The cross-section of the ventilation shaft was taken according to the actual dimensions, with a width of 7.9 m and a height of 7.0 m. The boundary conditions of the model were as follows: the bottom was fixed, constraining the normal deformation of the model's sides, and the top was a free surface. The cross-section at 80 m along the model's length (the junction of full-section excavation and TBM pilot tunnel excavation) was set as the analysis section to study the mechanical behavior of the surrounding rock at the junction.

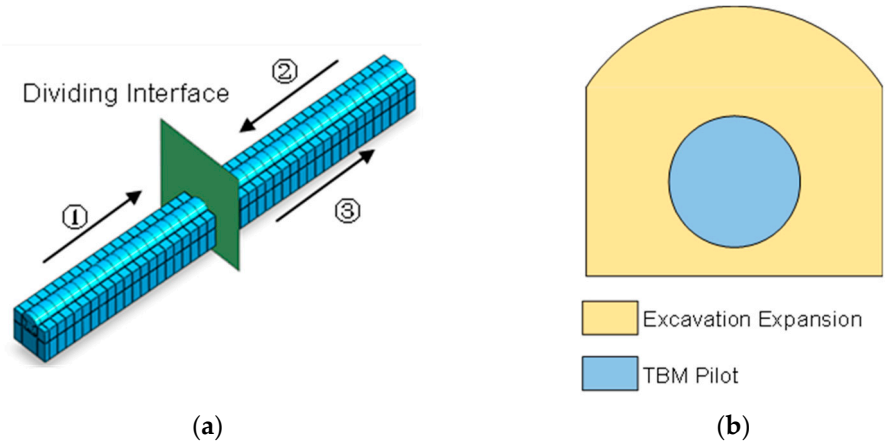

Figure 6. Schematic diagram of the construction process and pilot tunnel: (**a**) schematic diagram of the construction process, and (**b**) schematic diagram of the pilot tunnel.

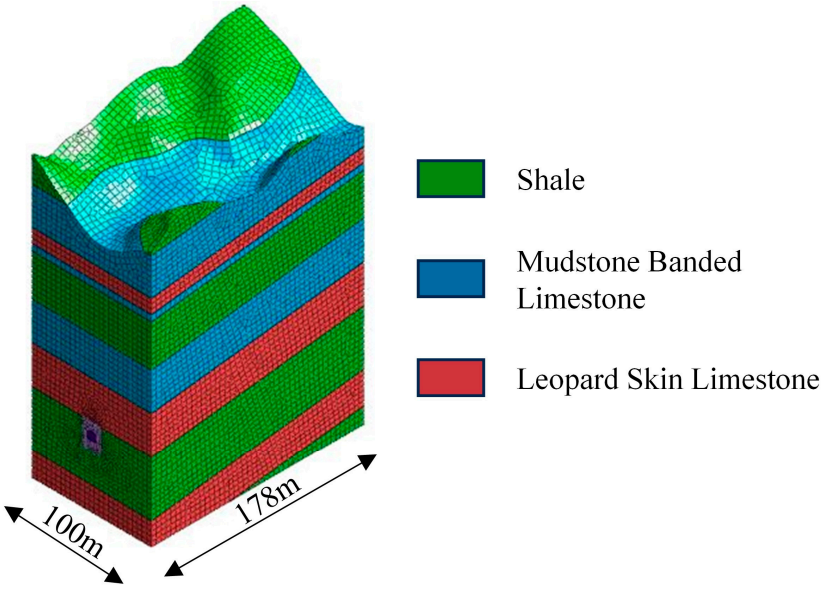

Figure 7. Mesh partition for computational model.

The surrounding rock was simulated using solid elements following the Mohr–Coulomb criterion, and shotcrete was simulated using plate elements. The concrete thickness for the full-section excavation was 100 mm, and for the TBM pilot tunnel excavation it was 200 mm. I18 Steel arches with a spacing of 750 mm were installed in this section, and the flexural stiffness of the steel arches was converted to the concrete [28]. The anchor bolts were simulated using embedded truss elements. The specifications of the anchor bolts in the fully excavated section were Φ22 mm × 3000 mm, with a spacing of 2000 mm × 2000 mm between the arch and the sidewall. In the TBM-driven tunnel section, the anchor bolts had specifications of Φ25 mm × 4000 mm, with a spacing of 1250 mm × 1250 mm between the arch and the sidewall. The mechanical parameters of the surrounding rock and support are provided in Table 4, and Figure 8 illustrates the schematic diagram of the modified rock mass parameters.

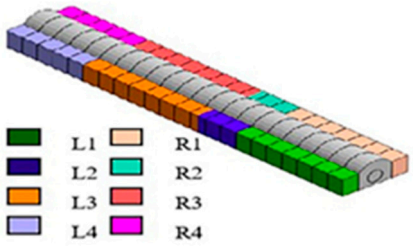

Figure 8. Schematic diagram of the corrected rock parameters.

5.2. Ventilation Shaft Deformation Analysis

Three indicators, namely the ventilation shaft deformation, the principal stresses of the surrounding rock, and the existing state of the surrounding rock, were analyzed to study the mechanical characteristics of the surrounding rock at the junction of the full-section excavation and TBM pilot tunnel excavation. The actual construction involves a daily advance of 4 m, corresponding to each construction step in the numerical simulation.

(1) Vertical Displacement of the Arch Top

The settlement data of the arch top at the end of each construction step for the analysis section were extracted to obtain the ventilation tunnel's arch settlement curve (Figure 9) and settlement table (Table 5). In Figure 9, the dashed line represents the beginning of a construction step. Taking the leftmost dashed line in Figure 9 as an example (denoted as S21 for the 21st excavation step), it represents the last excavation segment of the full-section construction.

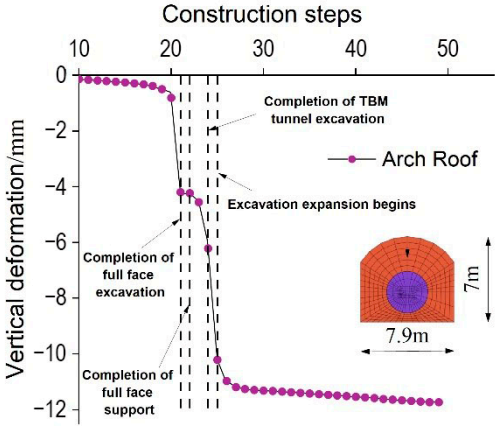

Figure 9. Curve of crown settlement.

Table 5. Table of vault settlements.

Construction Phase	Initial Settlement	Completion of Full Face Excavation	Completion of Full Face Support	Completion of TBM Tunnel Excavation	Excavation Expansion Begins
Settlement amount. (mm)	0.81	4.19	4.22	6.21	10.2
Final settlement. (mm)			11.73		
Settlement ratio.	6.91%	28.82%	0.26%	16.97%	34.02%

From Figure 9 and Table 5, it can be observed that the arch top settlement at the analysis section underwent five stages: initial settlement, accelerated deformation, slow deformation, abrupt deformation, and slow growth. Before the completion of the full-section excavation (before S21), the analysis section was influenced by the excavation of other parts of the surrounding rock, resulting in some initial settlement. However, due

to the distance between the excavation face and the analysis section (4 m and 16 m for the full-section excavation face and TBM pilot tunnel excavation face, respectively), the impact on the analysis section was limited, and the arch top settlement was only 0.81 mm, accounting for 6.91% of the total settlement. As the full-section excavation concluded (S21), the face became closer to the analysis section, and this construction segment was not supported after the excavation. Consequently, the arch top settlement experienced the first significant jump, reaching 4.19 mm. This stage accounted for 28.82% of the total settlement, indicating that the surrounding rock was in a state of accelerated deformation. When the full-section support was completed (S22), the TBM face continued to advance. At this point, the face was 8 m away from the analysis section, and the influence of the support at the full-section excavation on the surrounding rock at the TBM pilot tunnel excavation was limited. This resulted in a very small arch top settlement during this construction phase, with a final settlement of 4.22 mm, representing only 0.26% of the total settlement. The surrounding rock was in a state of slow deformation. When the TBM pilot tunnel excavation was completed (S24), the face reached the location of the analysis section. At this time, the arch top settlement increased to 6.21 mm, accounting for 16.97% of the total settlement. As excavation commenced (S25), the surrounding rock lost its constraint on the rock mass within the ventilation tunnel cross-section, leading to a rapid increase in deformation. The settlement reached 10.2 mm, accounting for 34.02% of the total settlement. The cumulative settlement at the end of the pilot tunnel excavation and the beginning of the enlargement accounted for 50.98% of the overall settlement, indicating that the surrounding rock was in a state of abrupt deformation. As the excavation face moved away from the analysis section and the support work was completed, the arch top settlement gradually increased to a stable state, with a final settlement of 11.73 mm.

(2) Horizontal Displacement of the Side Wall

The horizontal displacement at the middle point of the side wall at the end of each construction step for the analysis section was extracted to obtain the ventilation tunnel's side wall horizontal displacement curve (Figure 10). The dashed line in Figure 10 has the same meaning as that in Figure 9.

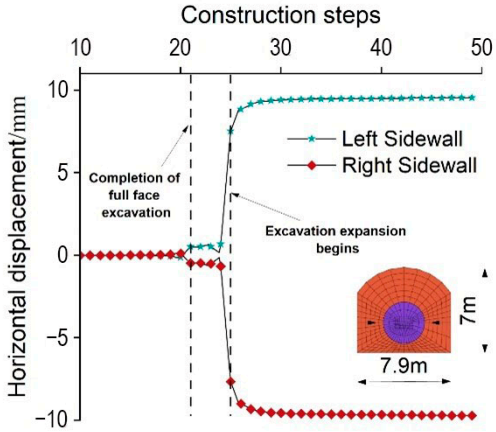

Figure 10. Horizontal displacement of the sidewall.

From Figure 10, the overall horizontal displacement curve exhibits an "S" shape. The horizontal displacements at the left and right wall measurement points are approximately equal. The final deformation at the left point is 9.55 mm and at the right point is −9.71 mm (with the negative indicating the negative direction of the coordinate axis). Both displacements represent compression deformations toward the interior of the ventilation tunnel. Before the completion of the full-section excavation (before S21), the construction of the ventilation tunnel had a minimal impact on the horizontal displacement at the analysis section, with a deformation of only 0.11 mm. As the full-section excavation ended and the TBM face progressed further (S21), the horizontal displacement of the side wall increased,

but the incremental deformation was small, with a final deformation of approximately 0.5 mm. During the subsequent construction steps (S22–S24, S22 involved the support construction of the full-section excavation, and S23–S24 only involved the TBM pilot tunnel excavation), the horizontal displacement of the side wall increased slowly, with a final deformation of only about 0.7 mm. This was because the area of the TBM pilot tunnel was smaller than that of the ventilation tunnel cross-section, and the unexcavated rock mass in the TBM pilot tunnel constrained the deformation of the surrounding rock at the measurement point, resulting in a small increase in horizontal displacement. As the excavation began (S25), the constraint of the rock mass disappeared, and the horizontal displacement of the side wall increased rapidly, reaching 7.52 mm. As the initial support for the enlargement was gradually completed, the rate of increase in horizontal displacement slowed down, eventually stabilizing.

From the ventilation tunnel deformation analysis, it can be seen that the deformations from S21 to S25 were the most intense throughout the entire construction process. Therefore, during excavation, attention should be paid to the blocks of surrounding rock formed by joint combinations, and reinforcement support should be carried out promptly and, if necessary, in advance.

5.3. Ventilation Tunnel Stress Analysis

As is well known, stress is a key factor affecting rock mass deformation. Referring to the results in Section 5.2, the stress variation pattern during the construction steps of the analysis section (S20–S25) was analyzed to reflect the mechanical state of the rock mass during construction. Since the maximum principal stress can comprehensively consider the distribution of vertical stress, horizontal stress, and shear stress in the surrounding rock, this section analyzed the stress state of the surrounding rock near the ventilation tunnel using the maximum principal stress. Figure 11 shows the contour plots of the maximum principal stress during the construction stages of S20–S25.

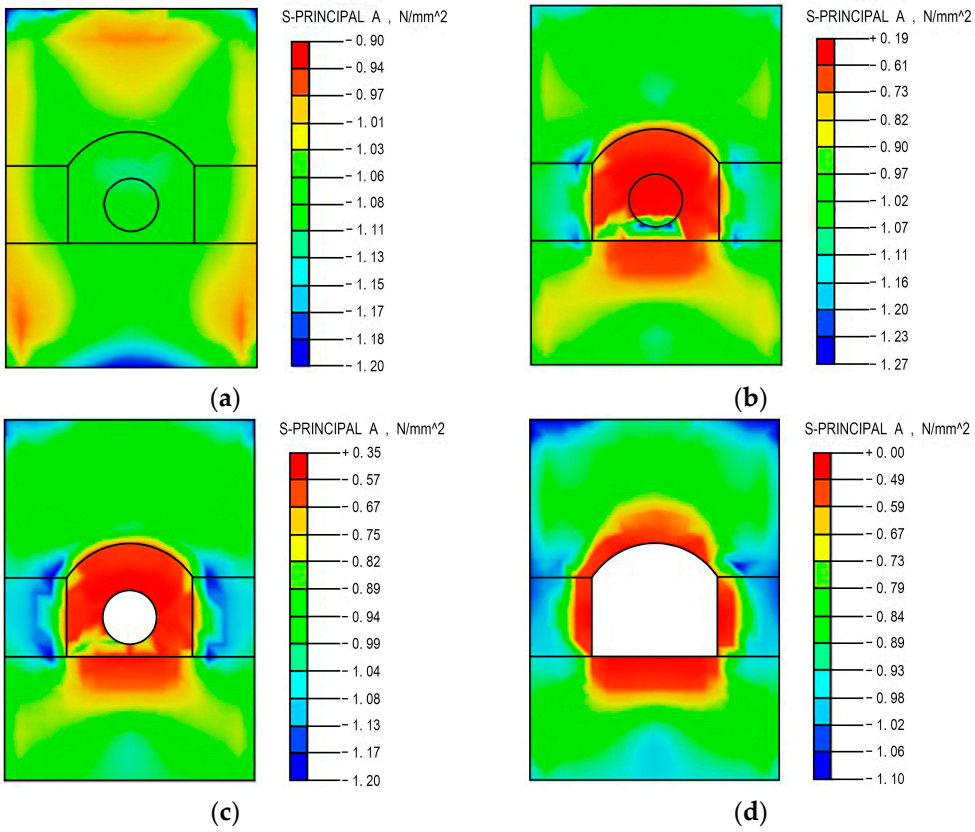

Figure 11. Contour of maximum principal stress: (**a**) S20, (**b**) S21, (**c**) S24, and (**d**) S25.

From Figure 11a, it can be seen that when the full-section excavation face is 4 m away from the junction interface and the TBM face is 16 m away, the overall rock mass surrounding the ventilation tunnel is under compression and the stress distribution is relatively uniform. The stress exhibits a "butterfly-shaped" symmetric distribution, with only a slight stress concentration above the outline of the pilot tunnel. The maximum principal stress value is around −1.25 MPa. Figure 11b shows that when the full-section excavation face advances to the junction interface, at which point the TBM face is 12 m away from the junction interface, the rock mass inside the ventilation tunnel outline changes from three-dimensional stress to two-dimensional stress. The rock mass experiences unloading effects and deforms toward the full-section excavation segment, causing tensile stress in the upper rock mass within the outline. The maximum tensile stress is 0.19 MPa. Additionally, stress concentration occurs at the junction interface, especially at the arch shoulder and bottom corner (blue area), where the maximum compressive stress is about 1.27 MPa. The stress distribution exhibits a "crescent moon" shape. This is mainly because, after the completion of the full-section excavation, the upper rock mass inside the outline transfers load forward, and the force flow intersects with the force flow transmitted downward by the rock mass at the arch shoulder, resulting in stress concentration in this part. The load at the arch shoulder is transmitted through the side wall, causing the side wall to move closer, while the rock mass inside the ventilation tunnel restrains the deformation of the side wall, subjecting it to a certain compression effect. The bottom corner is affected by the transmission of load and compression from the working face after the completion of the full-section excavation, leading to stress concentration in this part. In the subsequent construction process, due to the smaller size of the pilot tunnel compared to the overall size of the ventilation tunnel outline, the excavation of the pilot tunnel has a relatively small impact on the stress distribution and magnitude in the surrounding rock. The stress distribution in Figure 11c is similar to that in Figure 11b. In Figure 11c, when the TBM face advances to the junction interface, the tensile stress in the rock mass inside the ventilation tunnel outline further increases, with the maximum tensile stress reaching 0.35 MPa, appearing near the top of the TBM pilot tunnel. The arch shoulder and arch top are affected by the excavation of the pilot tunnel, resulting in tensile stress in the rock mass. The concentration of compressive stress is alleviated to a certain extent, and the maximum compressive stress decreases to 1.2 MPa. Figure 11d shows that as the excavation begins, the shallow rock mass near the ventilation tunnel outline is in a loose state. The range of loosening is greater on the left arch shoulder than on the right, and the loosening range of the roof and bottom is significantly greater than that of the side wall.

By analyzing the stress changes during the construction process at the analysis section, it is recommended to strengthen monitoring of the arch shoulder and bottom corner during construction. If the surrounding rock at these locations is relatively fragmented, reinforcement support, such as grouting rock bolts, can be applied to fill the fractures between rock masses, improve the strength of the surrounding rock, and enhance its bearing capacity.

5.4. Analysis of the Surrounding Rock's Existing State

The existing state of the surrounding rock can be represented by equivalent plastic strain, as shown in Figure 12.

In Figure 12a, when the full-section excavation face is 4 m away from the junction interface and the TBM face is 16 m away, the disturbance to the surrounding rock at the junction interface is minimal due to the distance between the working face and the junction interface. The equivalent plastic strain for the entire section is 0 (blue area). When the full-section excavation face reaches the junction interface, at which point the TBM face is 12 m away from the junction interface (Figure 12b), the rock mass at the junction interface inside the ventilation tunnel outline loses its constraint from the rock mass at the full-section excavation, leading to a change in the stress state. Plastic strain first appears inside the outline, with a larger plastic strain at the bottom of the pilot tunnel (red area), and the

shape of the entire plastic zone is similar to a butterfly. Since the area of the pilot tunnel is smaller than the area of the rock mass within the ventilation tunnel outline, the plastic zone undergoes almost no change during the excavation of the pilot tunnel, and the size and distribution of the equivalent plastic strain are almost the same as in Figure 12b. As the TBM face advances to the junction interface (Figure 12c), the plastic strain of the rock mass inside the ventilation tunnel outline increases, the concentration of plastic strain at the bottom edge of the pilot tunnel deepens, and the plastic zone extends to the outer edge of the side wall. There is little change in the plastic zone beneath the bottom plate. When the excavation is complete (Figure 12d), the plastic zone of the surrounding rock is concentrated from the bottom corner to the upper part of the arch shoulder. The plastic zone is approximately symmetrically distributed on the left and right sides. Due to the overall monoclinal structure of the surrounding rock, the left arch shoulder has a greater depth of plastic zone than the right side. The plastic strain and depth of the plastic zone on the side wall are significantly greater than those on the arch shoulder and bottom corner. The maximum plastic strain is located in the shallow rock mass at the middle of the side wall, and the maximum depth of the plastic zone is 2.2 m. With the application of support for the excavation section (Figure 12e), the plastic strain in the shallow rock mass of the side wall significantly decreases, and the maximum depth of the plastic zone in the side wall also decreases from 2.2 m to 1.9 m. The maximum depth of the plastic zone in the arch shoulder and its upper surrounding rock also decreases from 1.7 m to 1.5 m. The maximum expansion depth of the shoulder and its upper surrounding rock has decreased from 1.7 m to 1.5 m, indicating that the application of support has altered the stress state of the surrounding rock, effectively suppressing its deformation. As the excavation face gradually moves away from the boundary interface (Figure 12f), the disturbance of the surrounding rock at the interface by the construction is minimal. Consequently, the existing state of the surrounding rock at the interface has undergone almost no change.

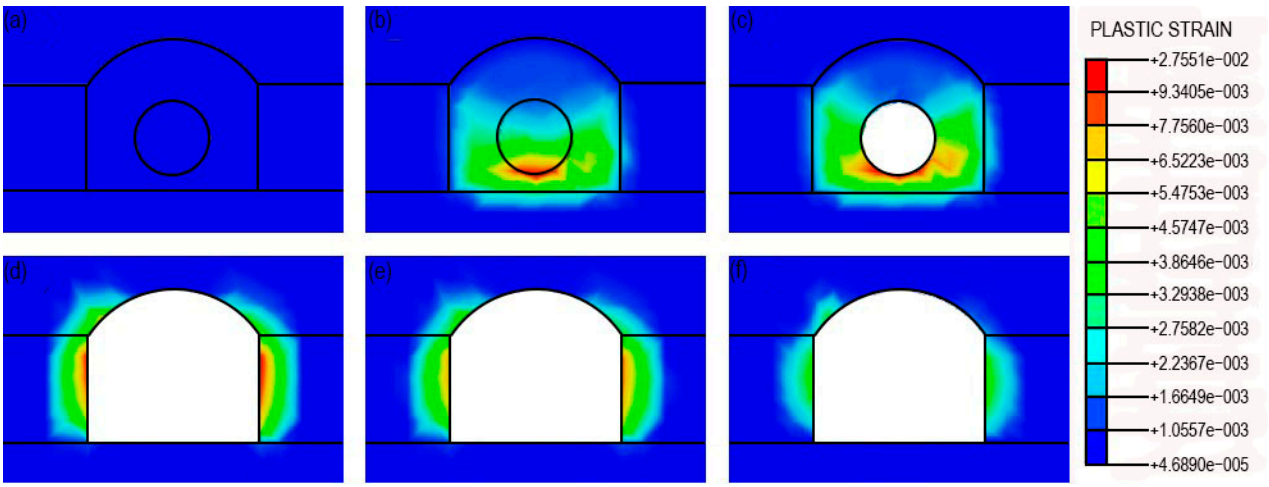

Figure 12. Distribution of the plastic zone: (**a**) S20, (**b**) S21, (**c**) S24, (**d**) S25, (**e**) S26, and (**f**) S30.

Through an analysis of the expansion pattern of the plastic zone, it is recommended to pay attention to monitoring the shoulder and sidewall during construction. When necessary, improvements to the stress state of the surrounding rock can be achieved by increasing the density of anchor rods.

6. Conclusions

This study, based on the construction project of the ventilation tunnel in the Wuhai Pumped Storage Power Station, employs TGP sidewall forecasting and wave velocity-based rock mass parameter predictions to systematically investigate the mechanical characteristics of the surrounding rock during construction. The following conclusions are drawn:

(1) TGP side wall prediction can provide the more accurate location of joint fractures, compensating for the deficiencies in geological surveying.
(2) The cumulative deformation of the ventilation tunnel during the excavation and expansion phases accounts for more than half of the total deformation. It is advised to enhance monitoring during excavation, promptly reinforce support, and implement advanced support when necessary.
(3) During expansion, there is a certain degree of stress concentration in the shoulder and bottom corner. Strengthening the monitoring of the shoulder and bottom corner during construction is recommended. If the surrounding rock in certain construction sections of the shoulder and bottom corner is relatively fragmented, enhancing the rock mass strength by injecting grouting anchors is suggested.
(4) Prior to expansion, the plastic zone primarily concentrates within the ventilation tunnel outline. Post-expansion, the plastic zone predominantly focuses on the sidewall and shoulder, influenced by the inclined structure of the surrounding rock. The expansion range of the left-side plastic zone is slightly larger than the right side. It is advised to enhance monitoring during construction and control plastic zone expansion by increasing the anchor rod density when necessary.
(5) This study primarily investigates the mechanical characteristics of surrounding rock during construction by estimating the rock mass mechanical parameters using wave velocity. However, the information concerning the structural planes in geological forecasting has not been incorporated into the numerical model. Therefore, considering the influence of structural planes on the stability of surrounding rock is the next step that needs to be carried out.

Author Contributions: Conceptualization C.F., G.W. and J.Q.; methodology C.F.; formal analysis C.F. and G.W.; resources G.W.; data curation C.F. and G.W.; writing—original draft C.F.; writing—review and editing J.Q.; visualization C.F.; supervision J.Q.; project administration G.W.; funding acquisition J.Q. and G.W. All authors have read and agreed to the published version of the manuscript.

Funding: This research was funded by the National Natural Science Foundation of China, grant number U1839202, Foundation of Key Laboratory for Prediction and Control on Complicated Structure System of the Education Department of Liaoning Province, grant number DLSZD2023[010] and the APC was funded by J.Q. and G.W.

Institutional Review Board Statement: Not applicable.

Informed Consent Statement: Not applicable.

Data Availability Statement: Data are contained within the article.

Conflicts of Interest: The authors declare no conflicts of interest.

References

1. Liu, F.; Che, Y.; Tian, X.; Xu, D.; Zhou, H.; Li, Z. Cost sharing mechanisms of pumped storage stations in the new-type power system: Review and prospect. *J. Shanghai Jiaotong Univ.* **2023**, *57*, 757–768.
2. Li, Z.; Xu, G.; Dong, J.; Li, Z.; Wang, J.; Chen, C. Deformation and fracture of surrounding rock mass of underground caverns at Houziyan hydropower station. *Chin. J. Rock Mech. Eng.* **2014**, *33*, 2291–2300.
3. Zhang, D.; Li, S.; Xu, D.; Li, Y.; Jiang, Q.; Xia, Y.; Li, Z. Investigation on deformation and cracking behaviors and stability analysis of surrounding rock mass of underground main powerhouse of Shuangjiangkou hydropower station during preliminary excavation. *Chin. J. Rock Mech. Eng.* **2021**, *40*, 520–532.
4. Meng, G.; He, S.; Chen, J.; Wu, J.; Chen, P.; Duan, X. Mechanism of deep deformation of roof arch of underground powerhouse at right bank of Baihetan hydropower station. *Chin. J. Geotech. Eng.* **2020**, *42*, 576–583.
5. Li, T.; Meng, L.; Zhu, J.; Li, Y.; Mou, L. Comprehensive analysis method for advanced forecast of geology in tunnels. *Chin. J. Rock Mech. Eng.* **2009**, *28*, 2429–2436.
6. Liu, C.; Liu, H.; Huang, Z. Analysis of surrounding rock anisotropy based on measured seismic wave velocity—A case study of Tingzhou Tunnel of Ganzhou-Longyan Railway. *Rock Soil Mech.* **2016**, *37*, 1451–1457.
7. Han, K.; Wang, B. Research on data analysis and detection technology of TSP advance forecast. *J. Railw. Eng. Soc.* **2020**, *37*, 72–77.
8. Luo, J.; Xu, J.; Chen, J. Application and research of comprehensive advanced geological prediction technology in tunnels. *J. Railw. Sci. Eng.* **2017**, *14*, 811–818.

9. Lu, Y.; Tan, X.; Guo, X.; Li, W. Estimation of rock mass shear strength parameters based on bore test and its application to engineering. *Chin. J. Rock Mech. Eng.* **2015**, *34*, 4116–4124.
10. Ding, W.; Yao, Z.; Jiang, Z. Study on method of how to select reasonably elastic wave velocity parameters of engineering rockmass. *Rock Soil Mech.* **2004**, *25*, 1353–1356.
11. Editorial Department of China Journal of Highway and Transport. Review on China's traffic tunnel engineering research:2022. *China J. Highw. Transp.* **2022**, *35*, 1–40.
12. Pelizza, S. Pilot bore excavation with TBM for the design and construction of larger tunnels. *Tunn. Undergr. Space Technol.* **1991**, *6*, 185–189. [CrossRef]
13. Zhou, J.; Yang, Z. Discussion on key issues of TBM construction for long and deep tunnels. *Rock Soil Mech.* **2014**, *35*, 299–305.
14. Ma, M.; Liu, W. Discussion on construction of long and large tunnels with TBM heading and enlargement method. *Railw. Stand. Des.* **2009**, *3*, 108–112.
15. Ding, X.; Wang, W.; Xi, W.; Han, C. Study on construction of Extra-long tunnels with TBM pilot and enlargement method. *Highway* **2023**, *68*, 63–68.
16. Zhu, Q. Discussion on the construction method for the Extra-long Shengli Road Tunnel in Tianshan. *Mod. Tunn. Technol.* **2020**, *57*, 175–179+185.
17. Wang, J.; Hu, J. Study on the effect of different TBM guideway locations on rock deformation around the hole. *Highway* **2021**, *66*, 374–377.
18. Wang, Z. Research on macroscopic quantitative relation between wave velocity and strength of rock (rock mass). *J. Railw. Eng. Soc.* **2011**, *28*, 6–9.
19. Li, G.; Xiong, C.; Li, N. Determination of Deformation Potential of Squeezed Surrounding Rock Tunnel. *J. Railw. Eng. Soc.* **2018**, *35*, 55–59.
20. Guo, Q.; Ge, X.; Che, A. Research on relationship of rock mass integrity index and rock mass elastic modulus. *Chin. J. Rock Mech. Eng.* **2011**, *30*, 3914–3919.
21. Hoek, E.; Carranza-Torres, C.; Corkum, B. Hoek-Brown failure criterion-2002 edition. In Proceedings of the Fifth North American Rock Mechanics Symposium, Toronto, ON, Canada, 7–10 July 2002; Volume 1, pp. 267–273.
22. Li, S.; Xue, Y. Modification of Hoek-Brown criterion and its application. *Chin. J. Rock Mech. Eng.* **2016**, *35*, 2732–2738.
23. Marions, P.; Hoek, E. GSI: A geologically friendly tool for rock mass strength estimation. In Proceedings of the GeoEng 2000 at the International Conference on Geotechnical and Geological Engineering, Melbourne, Australia, 19–24 November 2000.
24. Zuo, J.; Zuo, S.; Sun, Y.; Shi, Y.; Mi, C.; Li, Z. Wave velocity characterization and its correlation with physical parameters of overlying strata at different depth in Ningtiaota mine. *J. Min. Saf. Eng.* **2021**, *38*, 791–799.
25. Tang, D.; Zeng, J.; Hu, Y.; Chen, M. Discussion on testing and interpretation for Poisson's ratio. *Chin. J. Rock Mech. Eng.* **2001**, *20*, 1772–1775.
26. Huang, J.; Liu, N.; Ma, Z.; Lu, L.; Dang, K. The construction stability of large section tunnel considering the deterioration of clay mechanical properties. *Front. Mater.* **2023**, *10*, 1135276. [CrossRef]
27. Man, J.; Zhou, M.; Zhang, D.; Huang, H.; Chen, J. Face stability analysis of circular tunnels in layered rock masses using the upper bound theorem. *J. Rock Mech. Geotech.* **2022**, *14*, 1836–1848. [CrossRef]
28. Guo, H.; Chou, W.; Niu, X.; Zhang, H. Construction influence range of a new passgeway closely undercrossing a subway station. *Chin. Civ. Eng. J.* **2021**, *54*, 113–120.